Magnetic-resonance imaging techniques for detection of elasticity variation

J. B. Fowlkes
Department of Radiology, University of Michigan Medical Center, Ann Arbor, Michigan 48109-0553

S. Y. Emelianov
Institute of Mathematical Problems in Biology, Russian Academy of Sciences, Pushchino, 142292, Russia, Department of Radiology, University of Michigan Medical Center, Ann Arbor, Michigan 48109-0553 and Bioengineering Program and Department of Electrical Engineering and Computer Science, University of Michigan, Ann Arbor, Michigan 48109-2125

J. G. Pipe
Department of Radiology, University of Michigan Medical Center, Ann Arbor, Michigan 48109-0553

A. R. Skovoroda
Institute of Mathematical Problems in Biology, Russian Academy of Sciences, Pushchino, 142292, Russia

P. L. Carson and R. S. Adler
Department of Radiology, University of Michigan Medical Center, Ann Arbor, Michigan 48109-0553

A. P. Sarvazyan[a)]
Department of Chemistry, Rutgers University, New Brunswick, New Jersey 08903

(Received 19 July 1994; resubmitted 30 December 1994; accepted for publication 21 April 1995)

The relative success of manual palpation in the detection of breast cancer would suggest that a method for remote palpation resulting in a measurement of tissue elasticity could provide a diagnostic tool for detecting cancerous lesions deeper within the breast. This presumption is based in part on the excellent contrast between neoplastic and normal tissue due to the large (orders of magnitude) relative variation in the shear elastic modulus. By comparison, the bulk deformational modulus maintains the same value to within 20% for most soft tissues. A specific method of magnetic-resonance imaging (MRI) which measures tissue displacements has been used in experiments with a phantom containing regions of increased Young's modulus as a demonstration. The spatial modulation of magnetization technique uses the displacement of a spatial grid pattern caused by spin saturation to track regional motion. Mathematical reconstruction of the distribution of elastic moduli is shown for select examples. Any modality, e.g., MRI, ultrasound, etc., which can detect local tissue motion with sufficient spatial resolution can be used and therefore the results presented here should give an indication of the utility of such motion tracking techniques to future measurement of tissue elasticity.

I. INTRODUCTION

The evaluation of the elastic properties of tissues has the potential for being an important diagnostic tool in the detection of cancer as well as other injuries and diseases. The success of breast self-examination in conjunction with mammography for detection and continuous monitoring of lesions has resulted in early diagnosis and institution of therapy.[1,2] Self-examination is based on the manually palpable texture difference of the lesion relative to adjacent tissue and, as such, is limited to lesions located relatively near the skin surface and increased lesion hardness with respect to the surrounding tissue. Measurement of tissue "hardness" should allow more sensitive detection of abnormal structures deeper within tissue. Tissue hardness can actually be quantified in terms of the tissue elastic moduli and may provide excellent contrast between normal and abnormal tissues based on the large (orders of magnitude) relative variation in shear (or Young's) elastic modulus.

All of the commonly used medical imaging modalities can provide useful information about various tissue properties. Ultrasound relies primarily on the heterogeneity of acoustical impedance, which is a combination of the bulk modulus and the tissue density, CT scans depict the spatial distribution of x-ray attenuation, basically electron density which generally correlates with the physical density distribution. The tissue properties which provide contrast in MRI are better described microscopically and this contrast is very sensitive to water and fat content. However, the tissue properties which are being measured by most conventional imaging techniques, such as MRI, do not directly include the elasticity, which corresponds closely to the property of hardness obtained by the manual palpation.

The information which can be provided by developing an elasticity imaging technique is therefore complementary to that from other imaging modalities. The ability to take advantage of the additional data provided by tissue elastic properties is dictated by the tissue properties themselves and the spatial variation of these properties with respect to the inherent resolution of the imaging modality. However, processing of preimage information, such as the phase of the rf signal used in ultrasound imaging, may provide deformation measurements with better spatial resolution than that of the images normally produced.

In general, there are two approaches to remote measurements of tissue elasticity from standard imaging modalities. First, the elastic modulus can be determined for an internal tissue structure having boundaries detectable by an imaging modality. The motion of these boundaries is measured under

 0094-2405/95/22(11)/1771/8/$6.00

internal or external mechanical stress to evaluate the elastic properties of these structures.[3] The second approach is to evaluate the relative motion of tissue elements which are not separately resolvable by an imaging technique. Again the reconstruction of the elastic properties of tissue is based on an analysis of a motion pattern induced by internal or external stress.

There have been a number of experiments using ultrasonic techniques to measure tissue elasticity using both first and second approaches. For example, the presence of hard lesions can be detected using the measurement of Doppler-shift signals for tissue being mechanically vibrated using an external source.[4–7] Similarly, a number of other examples of tissue motion evaluation by Doppler measurements have been made.[8–10] Cross-correlation techniques have also been applied to both raw and envelope-detected rf data for the determination of tissue motion. Tristam *et al.*[11] were able to discriminate normal liver parenchyma from hepatic metastasis using a multidimensional evaluation of Fourier coefficients associated with the cross correlation. O'Donnell *et al.*[12] have also developed Fourier-based algorithms for the tracking of the arterial wall motion which demonstrate a tissue motion variation in the vicinity of harder plaques. This technique has been later used for accurate measurements of internal strain and displacement[13,14] with subsequent reconstruction of relative elastic Young's modulus[15] and others have used similar ultrasonic techniques to measure tissue displacements.[16] The imaging of tissue elastic properties using cross-correlation techniques has now developed to the point where 1D evaluation of tissue motion has been effectively demonstrated to produce 2D strain images related to elasticity distribution, so-called elastography.[17,18] The spatial variation in tissue elastic properties has also been evaluated using cardiac motion as a naturally occurring motion source in the prediction of fetal lung maturity[19,20] and in echocardiography.[21] In the former, *M*-mode images were analyzed to track the motion of specular reflectors during the cardiac cycle and the latter utilizes optical flow techniques.[22]

Finally, there have been independent methods for measuring the shear modulus which used actual shear wave propagation. These include work by Sarvazyan *et al.*[23,24] where a device is described which uses the propagation of a vibratory pulse to characterize tissue elasticity.

The measurement of tissue deformation using MRI has only recently been addressed in the literature, although several techniques for measuring bulk motion exist. Perhaps the most standard techniques involve the addition of a magnetic-field gradient to standard imaging sequences. This "motion sensitive gradient" is the cause of an additional phase shift in the MR signal of a voxel which is proportional to the motion of that voxel in the direction of the applied gradient field. With simple assumptions about the motion (e.g., constant velocity), the degree of motion is easily extracted from the phase information and the sequence parameters. In order to avoid aliasing (i.e., phase shifts $>2\pi$), the gradient strength must be chosen according to the velocity range being investigated. In addition, motion artifacts due to nonsystematic motion are likely to be enhanced in these methods. Some researchers[25,26] have demonstrated an extension of this technique designed to give the Fourier components of motion. Decorps and Bourgeois[27] have developed a different technique which correlates the actual MR signal intensity to motion. The nonlinear relationship between signal intensity and motion requires the setting of sequence parameters to target a specific range of motion. A recent method for measuring motion introduced by Zerhouni *et al.*[28] and extended by Axel and Dougherty[29] involves "tagging" tissue by selectively saturating the NMR signal available in that tissue. This saturation pulse can be applied in a variety of patterns which result in the appearance of radial or parallel lines or rectangular grids of low (saturated) signal intensity over an entire imaging slice. Tissue displacement after the application of this saturation pattern and before the acquisition of MRI data will result in a geometric distortion of that pattern, which can then be measured in the MR image. It is a specific implementation of this saturation pattern technique[30] which is used in the MRI experiments presented here. Finally, Young *et al.*[31] have applied signal saturation techniques to the materials testing problem by evaluation of the motion under specific application of shear stress.

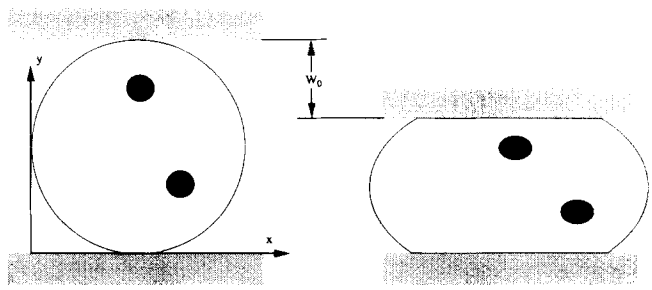

FIG. 1. A depiction of the phantom before and after deformation during both MRI experiments. The x and y axes indicate the spatial dimension along which the displacement is measured. W_0 is the absolute displacement of the deformation plate from its original position.

II. MATERIALS AND METHODS

MRI experiments were performed using cylindrical phantoms containing inclusions which had shear moduli which differed from that of the surrounding material (see Fig. 1). The phantom was a silicone composite cylinder measuring 90 mm in length with an 85-mm diameter. Within the phantom were three smaller cylinders (9-mm diameter), referred to as inclusions, all having a shear modulus approximately 10× greater than the background. Two of these cylinders were parallel to the central axis of the phantom and the other was positioned diagonally from one end of the phantom through approximately one-half of the length. A true 3D spin-echo pulse sequence on a 2-T GE Omega MRI system was employed to obtain the image of the phantom shown in Fig. 2 where the cylinders described above as within the phantom are shown brighter than the surrounding material. The elastic properties of the phantom materials were evaluated on an MTS model 810 Materials Test System (MTS Systems Corp., Minneapolis, MN) using a constant deformation–displacement test. The test was performed on a separate cylindrical piece of the inclusion material and on the phantom as a whole where the contributions from the two

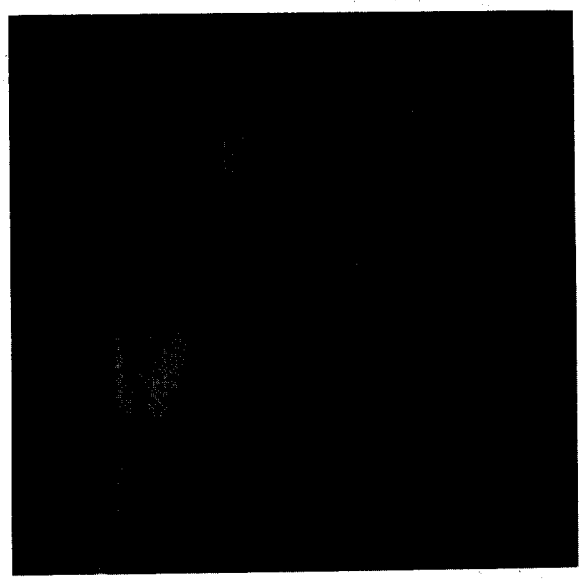

FIG. 2. An image of the test phantom used in deformation experiments. The image is reconstructed from a true 3D spin-echo pulse sequence. The phantom is composed of a large cylinder (85 mm in diameter and 90 mm in length) which surrounds three smaller cylinders (9 mm in diameter) termed "inclusions" and appearing as lighter outlines within the larger cylinder. Two of the smaller cylinders run the length of the phantom and the other runs at an angle from near one end of the phantom to a point halfway along one side. MR images during deformation studies were sagittal slices taken approximately 20 mm from the end of the phantom which is at the bottom of this figure and therefore away from the diagonal inclusion.

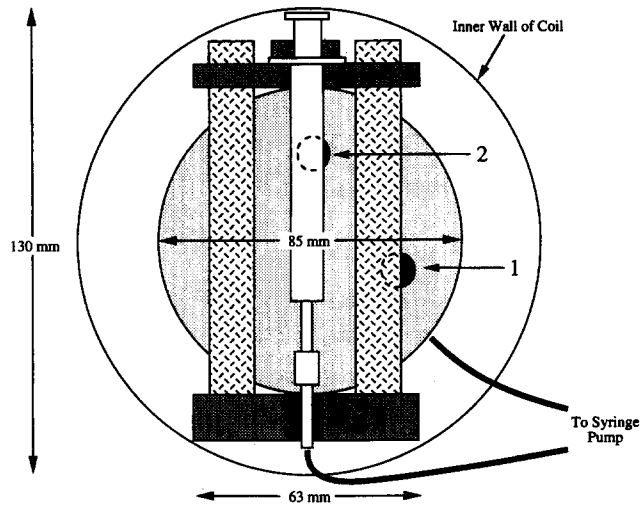

FIG. 3. A schematic of the deformation device used in the MRI experiments for detecting the inclusions numbered 1 and 2 in the figure. The phantom is placed between two plates where the top plate moves vertically along four rigid posts attached to the bottom plate. The motion is controlled by a hydraulic system composed of two syringes attached at either end of the top plate. The top of the syringe plungers contact the inside of the coil to force the top plate down to preset positions on mechanical stops. The restoring force of the phantom returns the top plate to its predeformation position. The syringes are filled manually using a single large syringe outside the magnet.

inclusions parallel to the central axis of the phantom were eliminated. The moduli ratio between the inclusion and its surrounding material was estimated to be 10.5 ± 1.5 for up to a 30% deformation of both materials.

Figure 3 is a diagram of the experimental deformation apparatus used to obtain MR images of the local displacements within the silicone phantom. For these deformation studies, the phantom was placed in the hydraulic device consisting of two plates whose vertical separation could be changed within 0.5 s under remote manual control. The phantom/deformation device was placed in a bird-cage coil and these together in the bore of the 2-T GE Omega MRI system. A uniform grid of coronal and sagital planes of NMR signal saturation was applied prior to an axial spin-echo image. The grid of saturation planes, applied using a spatial modulation of magnetization or SPAMM technique,[29,30] appears in the image as a grid of dark lines which has been predictably distorted by the deformation. The resulting deformation field contains local perturbations at the locations of the hard inclusions. Based on the pixel resolution (130-mm FOV and 256×256 image matrix), the grid spacing of 4 mm used in these experiments was within the guideline of greater than 5 pixels between tag lines suggested by other investigators.[32] The phantom was deformed vertically between application of the saturation planes and collection of the image data which were separated by 1 s. This time delay was sufficient for the deformation of the phantom to be complete (0.5 s) but short compared to the decay time for the saturation grid. The decay of the grid is exponential with a time constant of t/t_1 where t_1 spin-lattice relaxation time of the material which we empirically determined to be approximately 1 s. Therefore, for a 1-s delay, the grid would still be at $1/e$ of the initial differential between saturated and unsaturated material. As will be seen in Sec. III, the grid lines are still clearly visible in the SPAMM images. Tissue which might be of interest for this technique would include breast tissue which has t_1 values in the range of 800 ms for parenchymal tissue and carcinoma and significantly faster (~200–250 ms) for fat.[33] Although the t_1 for fat is short, the grid pattern would be retained in the other tissues for the time required for this SPAMM technique, particularly in denser (lower fat content) breasts which are the more problematic in mammography.

The SPAMM technique, as implemented here, involves the placement of a grid of saturation planes on the object prior to deformation and imaging. These saturation planes are applied in much the same way as a single slice is selected in conventional MR imaging. If one applies a magnetic-field gradient in a particular direction, a pulse of rf irradiation excites a slice profile similar to the Fourier transform of the rf pulse wave form. If only discrete samples of this rf wave form are used, then by basic sampling theory this slice profile is aliased into uniformly spaced repetitions of itself. In this manner two series of repetitive planes are placed orthogonally to each other and the imaging plane to produce an apparent grid of dark lines in the SPAMM image. If no motion occurs between the application of the saturation grid and image acquisition, the grid lines will be appear as uniform rectangles. If motion does occur, there will be a corresponding displacement of the grid lines which in turn reflects local displacements in the object. Note that this grid can be used to track in-plane motion only, but that through-plane motion will not appear to move the grid at all, and hence cannot be

detected with this original SPAMM technique. It is important to note that this technique does provide a full 2D deformation map similar to what might be expected for 2D displacement measurements for ultrasound imaging perhaps using a speckle tracking or monitoring of phase shifts in the ultrasound rf. However, a recent extension to SPAMM has been developed which allows the measurement of this third direction of motion,[30] giving a complete three-dimensional measure of displacement.

The mathematical formulation corresponding to the MRI experiments is given in the Appendix. The phantom is assumed to extend infinitely in the longitudinal direction so that the only nonzero components of the displacement are in the cross-sectional plane of the phantom. The inclusions were simulated as homogeneous cylinders with Young's moduli equal to 10× that of the surrounding material. The relative modulus values selected were based on the previously described deformation–displacement test of the elastic moduli for the phantom and inclusion materials. To analyze deformations of the phantom, the system of partial differential equations (A8) with proper boundary conditions (A7) has to be solved. Equations (A7) and (A8) represent a boundary-value problem and, because an analytical expression of the solution cannot be obtained for any given distribution of shear modulus G, numerical methods must be used. The system of equations (A7) and (A8) is solved using a method of finite differences with a second-order approximation to spatial derivatives. Another complication in the numerical computation is a boundary condition which cannot be predicted and must be also computed numerically. An iterative scheme is used to obtain the solution when the changing size of the loaded boundary, i.e., the deformation–dependent boundary condition (see Fig. 1) is taken into account in a step-wise fashion.[14]

In this study, a uniform, Cartesian discretization of 1.0 mm was used for the 85-mm-diameter cylindrical phantom. This size of a grid was chosen to properly represent all variations in the Young's modulus so that any further decrease in the grid itself will not change computed displacement fields. In the numerical scheme the iterations were continued until the mean-squared value of the relative displacements and pressure error was less than 10^{-6}.

III. RESULTS AND DISCUSSION

Figures 4(a) and 4(b) show the actual experimental results obtained in the MRI experiment where the first SPAMM image is prior to a forced surface displacement and the second is the deformed phantom. The slightly flattened appearance of the top and bottom of the phantom in Fig. 4(a) is due to gravity and initial preloading which was present prior to the plate displacement and application of the SPAMM grid when making displacement measurements. In Fig. 4(b), the top plate of the deformation system (Fig. 3) was displaced 25 mm with respect to the bottom plate (referred to as a 30% deformation) immediately prior to the SPAMM readout. Two regions of low signal intensity appear corresponding to the position of the inclusions. The inclusions have an increased cross linking in the silicone which may reduce the spin mobility within those regions and cause the inclusions to appear as low signal intensity circles in the image. The low signal intensity also reduces the ability to detect any shift of saturation lines within the inclusion. However, the deformation of the material surrounding the inclusion is sufficient to in-

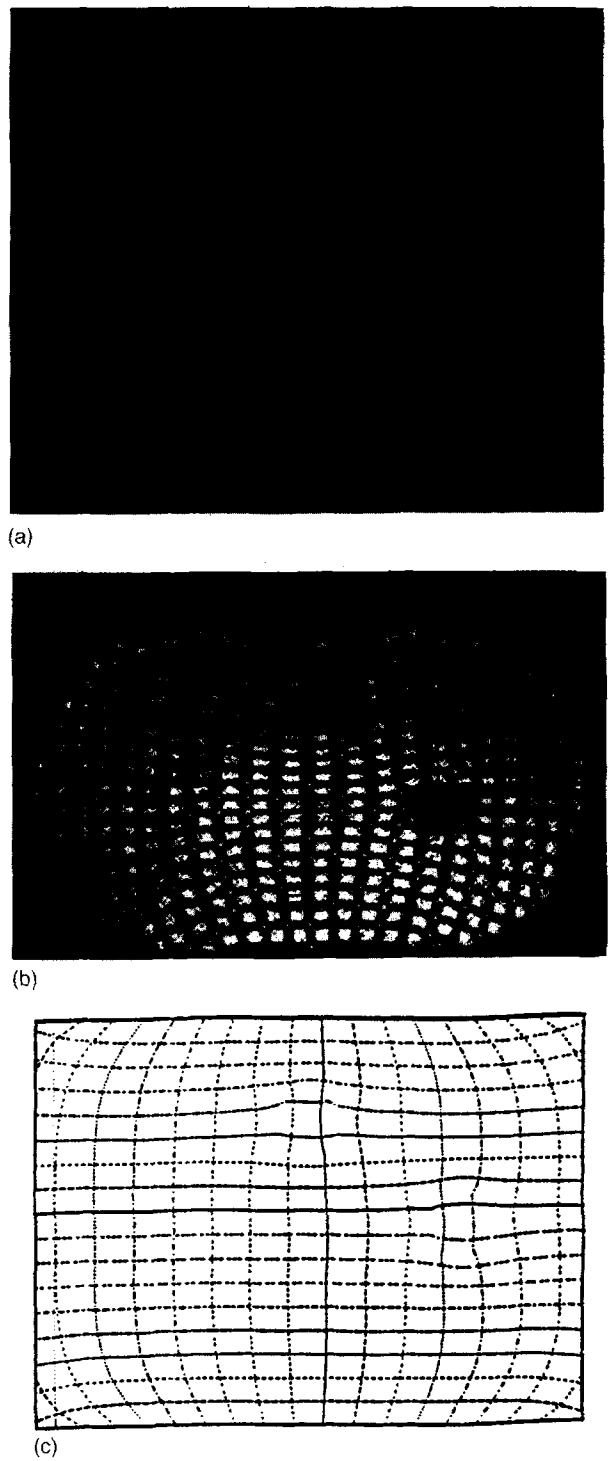

FIG. 4. MRI image of the 85-mm-diameter phantom with two 9-mm-diameter inclusions each with a shear modulus approximately 10× larger than that of the surrounding material. The inclusions appear as the low signal intensity circles in the image. (a) Before the deformation is applied the grid is rectangular and undistorted. (b) The grid lines reflect the deformation of the material when the phantom is deformed by 30%. (c) Mathematical simulation of the displacements for the central portion of the phantom in (b) near the inclusions.

dicate the presence of the local change of shear properties. It is also important to note that the inclusions deep within the phantom were not detected using manual palpation performed by several physicians familiar with the technique as applied in breast patients.

The theoretically predicted displacement pattern corresponding to the experimental results of Fig. 4(b) is presented in Fig. 4(c). A qualitative comparison of these figures shows a good agreement between theory and experiment. To quantitatively compare the experimental and theoretical results, the percent deformation was evaluated along vertical and horizontal lines passing through the center of each inclusion in the phantom. A selected group of these results is given in Figs. 5(a)–5(c). In each case the presence of the inclusion is indicated by a sudden decrease in the deformation at the position of the inclusion. The experimental measurements are consistent with the theoretical predictions for the positions of the inclusions and the magnitude of the percent deformation generally matches the theory quite well. In response to the localized reduction in deformation, the deformation for other portions of the phantom would increase. The evaluation along a line through the inclusion would be the equivalent to an ultrasound A-mode line measurement only with a spatial resolution of 4 mm in the case of MRI.

The effects of various parameters on inclusion detection are shown in Fig. 6. Consider the case of the cross-sectional (sagittal) view of the MRI phantom after deformation. Figure 6 is a theoretical prediction of the deformation expected for the case of an 18-mm-diameter circular inclusion within an 85-mm-diameter infinitely long cylinder being deformed in the fashion described in Fig. 1. In this way, the problem is reduced to a 2D geometry, ignoring the out-of-plane motion in the phantom (motion parallel to the longitudinal central axis of the cylinder). Note that for the 30% deformation of the phantom [Fig. 6(a)], the abnormal deformation about the inclusion is rather apparent. However, as indicated in Fig. 6(b), reducing the inclusion diameter by a factor of 2 results in a decreased deviation of the deformation making the inclusion more difficult to see. There are two ways to improve the detection of the smaller inclusion. First, the deformation of the material can be increased but, in some cases, increasing the deformation may not be possible because of the potential for the material to fail or for a transition to a highly nonlinear material response. In the case of medical applications, the deformation could also be limited by patient discomfort or other physical limitations. Therefore, the second option is to increase the grid resolution. The MR experiments presented here use a grid spacing of 4 mm as in the previous theoretical calculations. In Fig. 6(c), the resolution has been increased to 2 mm and two inclusions have been placed along the midline of the phantom to demonstrate the detection of multiple sites of varying moduli. There is an improvement in the visual detection of the inclusions as a result of the increased spatial resolution.

IV. SUMMARY

The MRI experiments presented here indicate that the SPAMM technique can be used to measure spatial variations

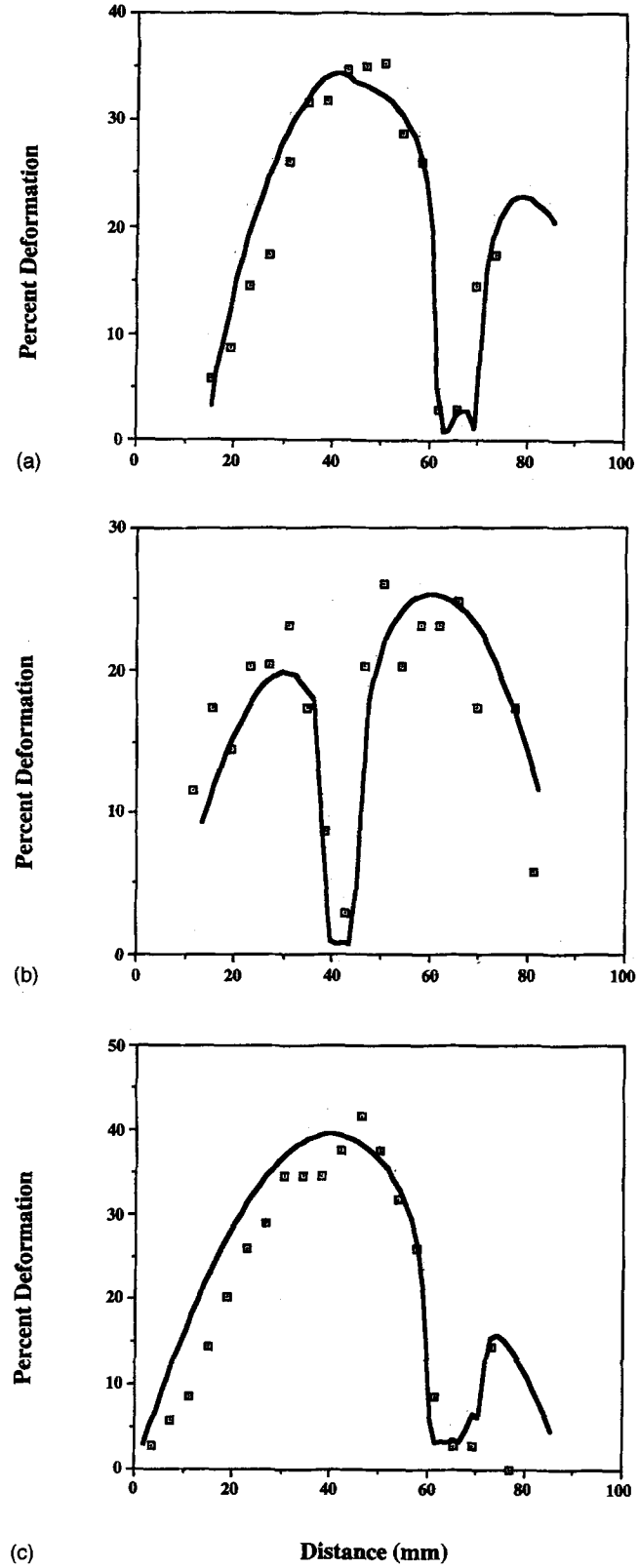

FIG. 5. Comparison of the percent deformation measured experimentally (points) and predicted theoretically (solid line). The comparison includes the deformation measured (a) perpendicular to a horizontal line through the center of inclusion 1 and plotted as a function of the position along this line; (b) and (c) parallel to a vertical line through the center of inclusion 1 and 2, respectively; and plotted as a function of the position along this line (see Fig. 3).

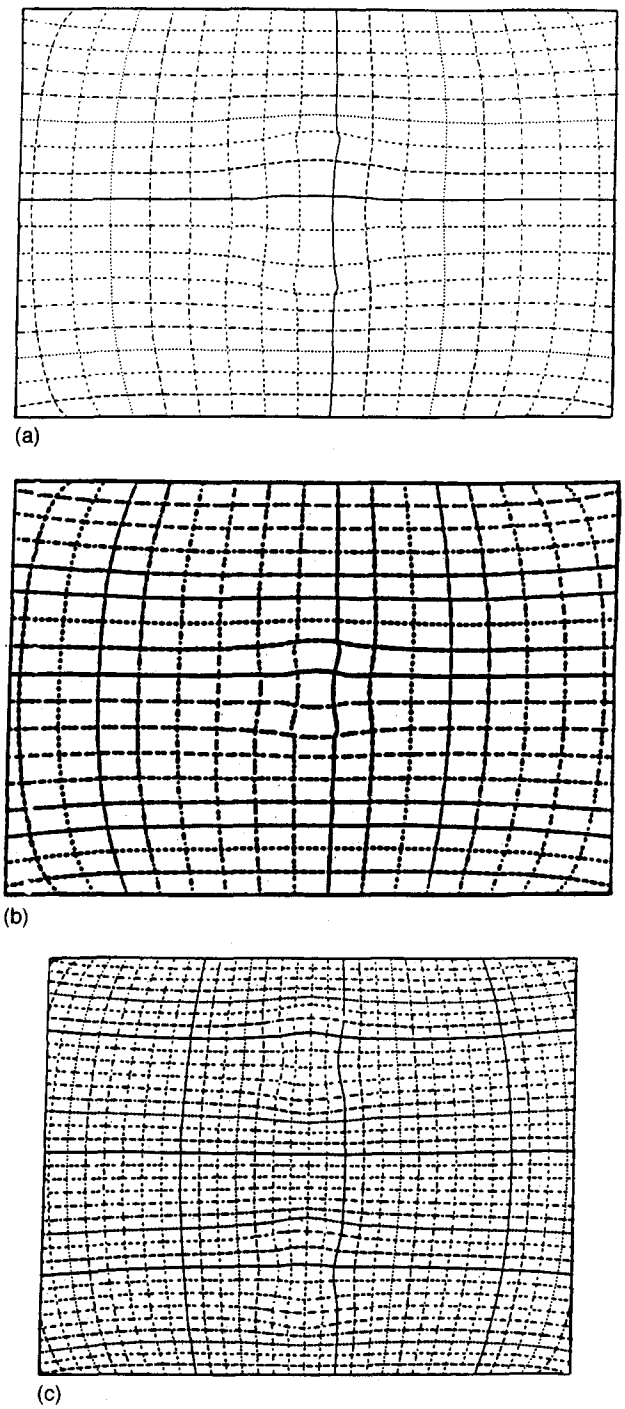

FIG. 6. Theoretical prediction of the displacement for the 85-mm-diameter phantom with an (a) 18 or (b) 9-mm-diameter circular inclusion, positioned in the center of phantom. The shear modulus of the inclusion is ~10× that of the surround material. The phantom is deformed by 30%, i.e., to 70% of its original diameter along the vertical direction. (c) Two 9-mm-diameter circular inclusions are distributed vertically along the central axis and the phantom is deformed by 30%. The spatial resolution here has also been increased by a factor of 2.

in deformation which result from the presence of localized regions of varying elastic moduli. The use of such measurement techniques in tissue could lead to the detection of hardness differences in tissue such as those used in detection of manually palpable masses in the breast. The possible advantages of this technique, however, may be access to deep, nonpalpable structures, quantitative estimation of the differences in tissue elasticity, resolution, and sensitivity of the proposed method, etc.

MRI elasticity imaging, in general, includes the following sequential procedures: measurement of the internal displacement field produced by internally or externally applied force, computation of all components of the strain tensor, and, finally, reconstruction of the tissue elasticity distribution based on these measurements. Therefore, sensitivity and resolution on the final elasticity distribution maps are not only imaging system dependent but also rely on mathematical models used to reconstruct the elasticity distribution, tissue properties, and type of external or internal deformation. These include specific characteristics of the mathematical model, shape, and relative size of the lesion compared to the spatial resolution of the imaging system, relative elasticity of the lesion compared to the "background" tissue, magnitude of the internal deformation, etc.

The mathematical model is an important consideration for elasticity imaging. The mathematical model based on linear elasticity and used in this study shows both qualitative and quantitative agreement with the experimental deformational data collected using MRI/SPAMM techniques. Even with a limited localization of a region differing in elastic properties, theoretical predictions indicate that the deformation of a tissue region surrounding a suspected lesion is sufficient for determining that the region contains abnormal tissue.

Using the same model, the resolution in elasticity imaging compared to the actual imaging system resolution can be illustrated by the following example. As it is shown elsewhere,[3] if a lesion only 3× "harder" than the surrounding tissue is isolated to a region with a radius 40% larger than its own, theory predicts that a 5% local deformation would be sufficient for lesion detection. Therefore, a 1-mm-diameter lesion measured within an imaging grid of 1.4 mm should be detectable using deformation techniques described here. Detection of lesions in this size range could greatly improve the early diagnosis of breast cancer. Note, also, that the required resolution of the imaging system can be even larger compared to that on the final elasticity images if the deformation magnitudes are increased, as illustrated in Fig. 6.

Finally, the mathematical techniques are applicable to any imaging modality which can produce a static or quasistatic deformation profile of the tissue and so measure a local deviation in deformation with sufficient resolution.

ACKNOWLEDGMENTS

The authors wish to acknowledge Dr. Matthew O'Donnell for his consultations on the MRI measurement of tissue motion.

APPENDIX: DESCRIPTION OF THEORETICAL MODEL

A theoretical model has been used for predicting strain patterns in a stressed material with spatially varying elastic properties and for solving the inverse problem of reconstructing the mechanical structure of an object from measure-

ments of the strain pattern. The theory is given in more detail elsewhere[34–36] and follows the work of Skovoroda.[14] Additionally, theoretical evaluations include potential optimization of parameters such as deformation techniques and measurement resolution. The model is formulated as a boundary-value problem with applied displacements on a piece of base material which contains inclusions having different elastic properties (henceforth called a phantom). The displacement field is taken to result from a known static surface deformation of the base material.

The equations of equilibrium of a body have the form

$$\sum_{n=1}^{3} \frac{\partial \sigma_{ij}}{\partial x_j} + f_i = 0, \quad i = 1,2,3, \tag{A1}$$

where f_i is the force per unit volume acting in the x_i direction, u_i is the particular displacement in the x_i direction, and σ_{ij} are the components of the stress tensor. In the general case of the linear elastic model of a *compressible* media, the stress–strain relations are described by the equation

$$\sigma_{ij} = (K - \tfrac{2}{3}G)\Theta\,\delta_{ij} + 2G\epsilon_{ij}, \tag{A2}$$

where K and G are bulk and shear moduli, respectively, δ_{ij} is Kronecker's delta symbol, ϵ_{ij} and Θ are the components and the trace of strain tensor, respectively, defined in the linear approach as

$$\epsilon_{ij} = \frac{1}{2}\left(\frac{\partial u_i}{\partial x_j} + \frac{\partial u_j}{\partial x_i}\right), \tag{A3}$$

$$\Theta = \sum_{i=1}^{3} \epsilon_{ii} = \epsilon_{11} + \epsilon_{22} + \epsilon_{33}. \tag{A4}$$

Since most of soft tissues are *incompressible*,[3] i.e., Poisson's ratio is very close to 0.5, the relations between stress and strain take the form[14]

$$\sigma_{ij} = p\,\delta_{ij} + 2G\epsilon_{ij}, \tag{A5}$$

where p is the static pressure. Incompressibility then yields the additional condition that

$$\epsilon_{11} + \epsilon_{22} + \epsilon_{33} = 0. \tag{A6}$$

Therefore, a closed set of coupled differential equations can be generated by combining Eqs. (A1) and (A3)–(A6) and eliminating stress and strain components. This system, however, has an infinite number of solutions, where the unique solution is determined by the boundary condition.

Generally the boundary conditions take the form

$$\left(\sum_j \sigma_{ij} n_j - F_i\right)\delta(u_i - u_i^0) = 0, \tag{A7}$$

where n_j is the jth component of a unit normal vector at the body surface, F_i is the force per unit area of the surface acting in the x_i direction, and δ is a symbol of the variation. If there are any known external forces F_i applied to part of the surface of the body, Eq. (A7) is satisfied for this part of the surface by means of the first term. If there are any known displacements u_i^0 of part of the body surface, Eq. (A7) is satisfied there by means of the second term.

In the present study 2D approximation has been used for a given geometry of the phantom and deformation load. With this assumption the closed set of coupled differential equations (A1) and (A3)–(A6) will take a form

$$\begin{aligned}
&\frac{\partial p}{\partial x_1} + 2\frac{\partial}{\partial x_1}\left(G\frac{\partial u_1}{\partial x_1}\right) + \frac{\partial}{\partial x_2}\left[G\left(\frac{\partial u_1}{\partial x_2} + \frac{\partial u_2}{\partial x_1}\right)\right] = 0,\\
&\frac{\partial p}{\partial x_2} + 2\frac{\partial}{\partial x_2}\left(G\frac{\partial u_2}{\partial x_2}\right) + \frac{\partial}{\partial x_1}\left[G\left(\frac{\partial u_1}{\partial x_2} + \frac{\partial u_2}{\partial x_1}\right)\right] + \rho g = 0,\\
&\frac{\partial u_1}{\partial x_1} + \frac{\partial u_2}{\partial x_2} = 0,
\end{aligned} \tag{A8}$$

where ρ is density of the phantom material and g is the gravitational acceleration. In system (A8) the first two equations are the equations of equilibrium (A1) written in terms of the displacement $u(x_1,x_2)$, pressure $p(x_1,x_2)$, and shear modulus $G(x_1,x_2)$, and the last equation is the condition of incompressibility (A6).

Finally, Eqs. (A8) with boundary condition (A7) represent a boundary-value problem and, in general, have no analytical solution for any given distribution of the shear modulus G, and therefore numerical methods must be used.

[a]Permanent address: Institute for Theoretical and Experimental Biophysics, Russian Academy of Sciences, Pushchino, 142292, Russia.

[1]D. Hill, V. White, D. Jolley, and K. Mapperson, "Self examination of the breast: is it beneficial? Meta-analysis of studies investigating breast self examination and extent of disease in patients with breast cancer," Br. J. Med. **297**, 271–275 (1988).

[2]P. A. Newcomb, S. Weiss, B. E. Storer, D. Scholes, and B. E. Young, "Breast self-examination in relation to the occurrence of advanced breast cancer," J. Natl. Cancer Inst. **83**, 260–265 (1991).

[3]A. P. Sarvazyan, A. R. Skovoroda, S. Y. Emelianov, J. B. Fowlkes, J. G. Pipe, R. S. Adler, R. B. Buxton, and P. L. Carson, "Biophysical bases of elasticity imaging," in *Acoustical Imaging*, edited by J. P. Jones (Plenum, New York, 1995), Vol. 21, pp. 223–240.

[4]R. M. Lerner and K. J. Parker, "Sono-elasticity in ultrasonic tissue characterization and echographic imaging," Proceedings of the 7th European Commission Workshop, edited by J. M. Thijssen, October 1987, Nijmegen, The Netherlands, 1987 (unpublished).

[5]K. J. Parker, S. R. Huang, R. A. Musulin, and R. M. Lerner, "Tissue response to mechanical vibrations for sonoelasticity imaging," Ultrasound Med. Biol. **16**, 241–246 (1990).

[6]R. M. Lerner, S. R. Huang, and K. J. Parker, "Sonoelasticity images derived from ultrasound signals in mechanically vibrated tissues," Ultrasound Med. Biol. **16**, 231–239 (1990).

[7]K. I. Parker and R. M. Lerner, "Sonoelasticity of organs: Shear waves ring a bell," J. Ultrasound Med. **11**, 387–392 (1992).

[8]X. T. Truong, S. R. Jarrett, M. C. Nguyen, "A method for deriving viscoelastic modulus from transient pulse propagation," IEEE Trans. Biomed. Eng. **BE-24**, 382–385 (1978).

[9]T. A. Krouskop, D. R. Dougherty, and S. F. Levinson, "A pulsed Doppler ultrasonic system for making non-invasive measurements of the mechanical properties of soft tissue," J. Rehabil. Res. Dev. **24**, 1–8 (1987).

[10]Y. Yamakoshi, J. Sato, and T. Sato, "Ultrasonic imaging of the internal vibration of soft tissue under forced vibration," IEEE Trans Ultrason. Ferroelectr. Frequency Control **UFFC-37**, 45–53 (1990).

[11]M. Tristam, D. C. Barbosa, D. O. Cosgrove, D. K. Nassiri, J. C. Bamber, C. R. Hill "Ultrasonic study of *in vivo* kinetic characteristics of human tissue," Ultrasound Med. Biol. **12**, 927–937 (1986).

[12]M. O'Donnell, A. R. Skovoroda, and B. M. Shapo, "Measurement of arterial wall motion using Fourier-based speckle tracking algorithms," *Proceedings of the 1991 IEEE Ultrasonics Symposium* (IEEE, Piscataway, NJ, 1991), Vol. 2, pp. 1101–1104.

[13]M. O'Donnell, A. R. Skovoroda, B. M. Shapo, and S. Y. Emelianov, "Internal displacement and strain imaging using ultrasound speckle tracking," IEEE Trans. Ultrason. Ferroelectr. Frequency Control **UFFC-41**, 314–325 (1994).

[14]A. R. Skovoroda, S. Y. Emelianov, M. A. Lubinski, A. P. Sarvazyan, and M. O'Donnell, "Theoretical analysis and verification of ultrasound displacement and stain imaging," IEEE Trans. Ultrason. Ferroelectr. Frequency Control **UFFC-41**, 302–313 (1994).

[15]S. Y. Emelianov, A. R. Skovoroda, M. A. Lubinski, and M. O'Donnell, "Reconstructive elasticity imaging," in *Acoustical Imaging*, edited by J. P. Jones (Plenum, New York, 1995), Vol. 21, pp. 241–252.

[16]L. S. Wilson and D. E. Robinson, "Ultrasonic measurement of small displacements and deformations of tissue," Ultrason. Imag. **4**, 71–82 (1982).

[17]J. Ophir, I. Cespedes, H. Ponnekanti, Y. Yazdi, X. Li, "Elastography: a quantitative method for imaging the elasticity of biological tissues," Ultrason. Imag. **13**, 111–134 (1991).

[18]I. Cespedes, J. Ophir, H. Ponnekanti, and N. Maklad, "Elastography: elasticity imaging using ultrasound with application to muscle and breast in vivo," Ultrason. Imag. **15**, 73–88 (1993).

[19]R. S. Adler, J. M. Rubin, P. H. Bland, and P. L. Carson, "Characterization of transmitted motion in fetal lung: Quantitative analysis," Med. Phys. **16**, 333–337 (1989).

[20]R. S. Adler, J. M. Rubin, P. H. Bland, and P. L. Carson, "Quantitative tissue motion analysis of digitized *M*-mode images: Gestational differences of fetal lung," Ultrasound Med. Biol. **16**, 561–569 (1990).

[21]J. Meunier, M. Bertrand, G. Mailloux, and R. Petitclerc, "Assessing local myocardial deformation from speckle tracking in echography," Proc. SPIE **914**, 20–29 (1988).

[22]K. P. Horn and B. G. Schunck, "Determining optical flow," Artif. Intell. **17**, 185–203 (1981).

[23]A. P. Sarvazyan, A. R. Skovoroda, and D. Vucelic, "Utilization of surface acoustic waves and shear acoustic properties for imaging and tissue characterization," in *Acoustic Imaging*, edited by H. Ermert and H. P. Harjes (Plenum, New York, 1992), Vol. 19, pp. 463–467.

[24]A. P. Sarvazyan, V. Ponomarjev, D. Vucelic, G. Popovic, and A. Veksler, "Method and device for acoustic testing of elasticity of biological tissues," US Patent No. 4,957,851 (14 August 1990).

[25]D. A. Feinberg, L. E. Crooks, P. Sheldon, J. Hoenninger, J. Watts, and M. Arakawa, "Magnetic resonance imaging the velocity vector components of fluid flow," Magn. Reson. Med. **2**, 555–566 (1985).

[26]D. A. Feinberg and P. D. Jakab, "Tissue perfusion in humans studied by Fourier velocity distribution, line scan, and echo-planar imaging," Magn. Reson. Med. **16**, 280–93 (1990).

[27]M. Decorps and D. Gourgeois, "Very slow flow imaging," Magn. Reson. Med. **19**, 270 (1991).

[28]E. A. Zerhouni, D. M. Parish, W. J. Rogers, A. Yang, and E. P. Shapiro, "Human heart: tagging with MR imaging—a method for noninvasive assessment of mycardial motion," Radiology **169**, 164–172 (1988).

[29]L. Axel and L. Dougherty, "Heart wall motion: improved method of spatial modulation of magnetization for MR imaging," Radiology **169**, 59–63 (1988).

[30]J. G. Pipe, J. L. Boes, and T. L. Chenevert, "Method for measuring three-dimensional motion with tagged MR imaging," Radiology **181**, 591–595 (1991).

[31]Y. A. Young, L. Axel, L. Dougherty, D. K. Bogen, C. S. Parenteau, "Validation of tagging with MR imaging to estimate material deformation," Radiology **188**, 101–108 (1993).

[32]R. Elliot and L. G. McVeigh, "Precision of tag position estimation in breath-hold CINE MRI: The Effect of Tag Spacing," Society of Magnetic Resonance in Medicine 12th Annual Scientific Meeting and Exhibition, New York, NY, 1993, Abstract No. 199 (unpublished).

[33]K. I. Dean and M. Komu, "Breast tumor imaging with ultra low field MRI," Magn. Reson. Imag. **12**, 395–401 (1994).

[34]L. D. Landau and E. M. Liftshitz, *Theory of Elasticity* (Nauka, Moscow, 1965).

[35]Y. N. Rabotnov, *Mechanics of solid structures* (Nauka, Moscow, 1979).

[36]G. E. Mase, *Schaum's Outline of Theory and Problems of Continuum Mechanics* (McGraw-Hill, New York, 1970).